Supporting Information for

Leveraging Pd(100)/SnO_2 Interfaces for Highly Efficient Electrochemical Formic Acid Oxidation

Haiyan Huang,[‡a] Tianyi Yang,[‡a] Fang Sun,[‡a] Zhaohui Liu,[a*] Qing Tang,[a*] Lingmei Liu,[a] Yu Han,[b] Jianfeng Huang[a*]

[a] State Key Laboratory of Coal Mine Disaster Dynamics and Control, School of Chemistry and Chemical Engineering, Institute of Advanced Interdisciplinary Studies, Chongqing 400044, China

[b] Advanced Membranes and Porous Materials Center, King Abdullah University of Science and Technology (KAUST), Thuwal 23955-6900, Saudi Arabia

Email: zhaohui.liu@cqu.edu.cn, qingtang@cqu.edu.cn, jianfeng.huang@cqu.edu.cn

Chemicals and Materials

D-(+)-glucose (99.5%), sodium stannate trihydrate ($Na_2SnO_3 \cdot 3H_2O$, 98%), sodium iodide (NaI, 99.5%), palladium (II) acetylacetonate ($Pd(acac)_2$, 99%), dimethyl Formamide (DMF, 99.5%), formic acid (HCOOH, 99.5%), hexadecyl trimethyl ammonium bromide (CTAB, 99%) and ascorbic acid (AA, 99%) were purchased from Shanghai Aladdin Biochemical Technology Co. Ltd. Pd/C was bought from Shanghai Macklin Biochemical Co., Ltd. Polyvinylpyrrolidone (PVP) K30, sodium hydroxide (NaOH, 98%) and perchloric acid ($HClO_4$, 70%) were obtained from Chengdu Kelong Chemical Co. High purity N_2 (99.999%) was purchased from Chongqing Rising gas Co. Ltd. All reagents were used as received without further purification. All aqueous solutions were prepared using deionized (DI) water with a resistivity of 18.2 MΩ·cm.

Characterizations

Electron Microscopy

Transmission electron microscopy (TEM), high-resolution TEM (HRTEM), high-angle annular dark-field scanning TEM (HAADF-STEM) images and X-ray energy dispersive (EDX) elemental mappings were acquired on Thermo Scientific, Talos-F200S at 200 kV. Specimens were prepared by depositing 15 μL particle dispersion on the surface of carbon-coated copper grids, followed with natural drying in air.

X-ray Diffractometry (XRD)

XRD measurements were conducted on a PANalytical X'Pert Powder Advance instrument with Cu K_α radiation. Samples were prepared by drop-casting nanoparticles on low background silicon plates. XRD patterns were recorded in the range of 10°−80° in a continuous scanning mode, with an increment of 4°/min.

X-ray Photoelectron Spectroscopy (XPS)

XPS data were collected on ESCALAB 250Xi with a monochromatic Al K_α X-ray source under ultrahigh vacuum conditions. Samples were prepared by drop-casting nanoparticles on silicon substrates to form a thin particle film. C_{1s} peak (284.6 eV) was used to calibrate the binding energy of other elements.

Inductively Coupled Plasma Optical Emission Spectrometry (ICP-OES)

ICP-OES was performed on Spectro GREEN model to determine the Pd concentration. Five standard solutions of varied Pd concentrations were prepared to obtain the calibration curves, based on which the concentrations of the digested solutions were determined. The sample solution was prepared by dissolving the nanoparticles in 70% HNO_3 followed by the addition of a specific amount of DI water to form a 2% acid solution for the analysis.

Computational Calculations

All the DFT calculations were implemented in the Vienna ab initio Simulation Package (VASP5.4.4) package.[1] The exchange-correlation interactions are modeled by the Perdew-Burke-Ernzerhof (PBE) function within the generalized gradient approximation (GGA), and the projector augmented-wave (PAW) method is carried out to describe the ion-electron interactions.[2, 3] The wave functions of all the computations were expanded via a plane-wave cutoff energy of 400 eV during the structural relaxation, and the Brillouin zone was sampled by 3×3×1 k-points by means of Monkhorst−Pack scheme. The convergence criteria for energy and force is set as 10^{-5} eV and 0.01 eV A^{-1} for maximal displacement, respectively. Along the perpendicular direction, a vacuum space at least 18 Å was added to eliminate the effects of periodic structure. In addition, we utilized the empirical density functional dispersion (DFT-D3) method[4] to consider the van der Waals interactions between adsorbate and interface.

The optimized bulk face centered cubic Pd structure has a lattice constant of 3.891 Å. The lattice constants for optimized bulk SnO_2 are a = 4.740 Å, b = 4.740, c = 3.19 Å. Predicted lattice constants for both materials deviate < 0.3% from their corresponding experimental values. The optimized bulk structures were used to construct surface slab models. The (3 × 3) Pd (100) and (111) slab models of four layers were used for pure Pd, with the bottom two layers of Pd atoms fixed to mimic bulk structure. For the hybrid model, a two-layer (5 × 2) SnO_2 (110) slab was constructed, with the bottom one layer fixed and an Pd nanoparticle (NP) placed on top. The Pd NP consists of two layers of (3 × 3) Pd (100) or (111), with Pd termination interacting with SnO_2 (110) surface to make an effective interface.

Based on the computational hydrogen electrode (CHE) model,[5] the change of Gibbs free energy for each formic acid decomposition elementary reaction can be calculated as:

$$\Delta G = \Delta E + \Delta ZPE - T\Delta S$$

Where ΔE, ΔZPE and ΔS are the change of the total energy that can be directly obtained from DFT calculations, the difference of zero-point energy, and the change of entropy at 298.15 K, respectively.

Supporting Figures

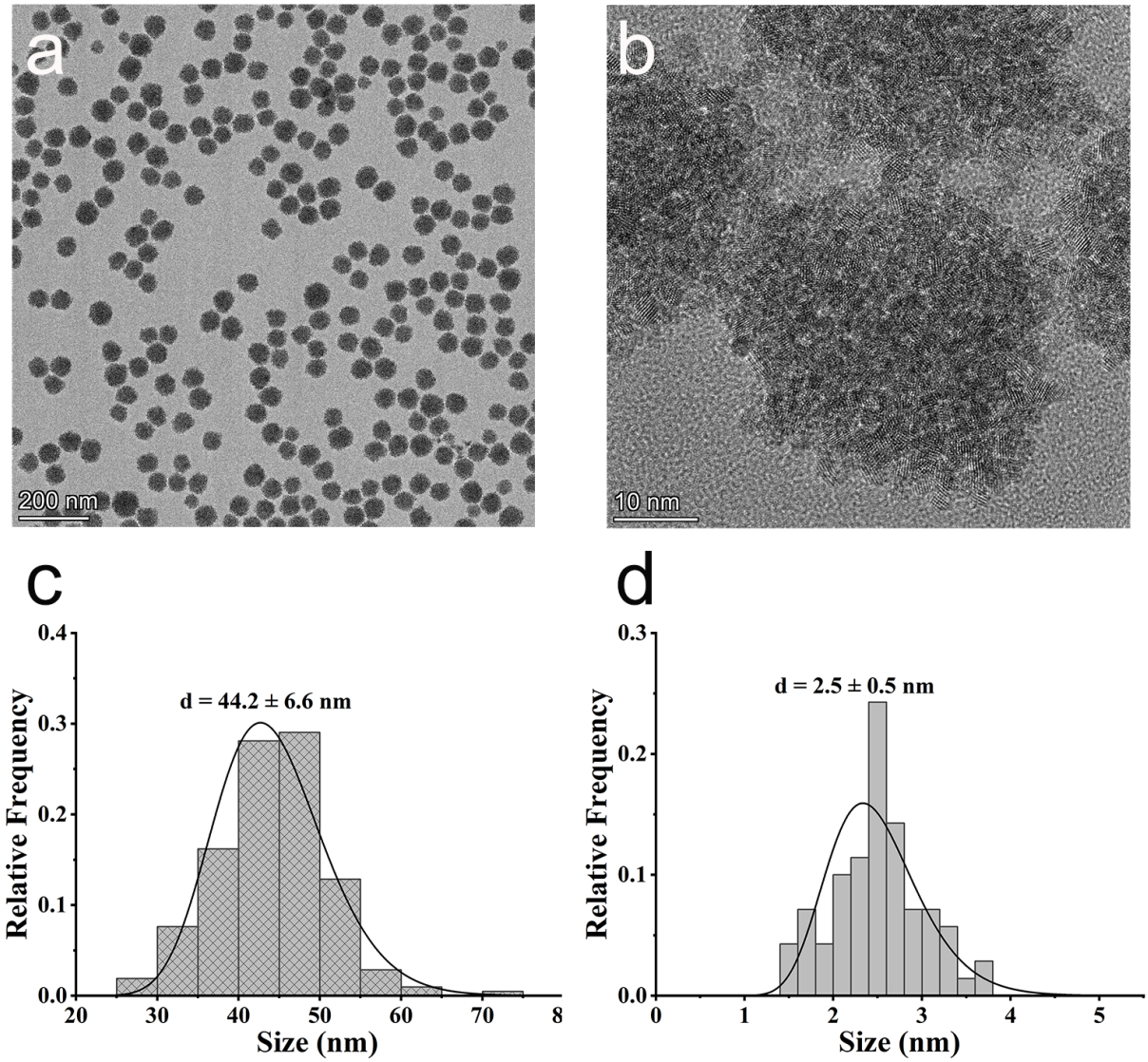

Fig. S1 (a) TEM and (b) HRTEM images of SnO_2 nanospheres used as seeds for the synthesis of *h*-PdNCs@SnO_2 in this work. (c, d) Statistic histograms showing the average (c) particle size and (d) crystallite size of SnO_2 nanospheres.

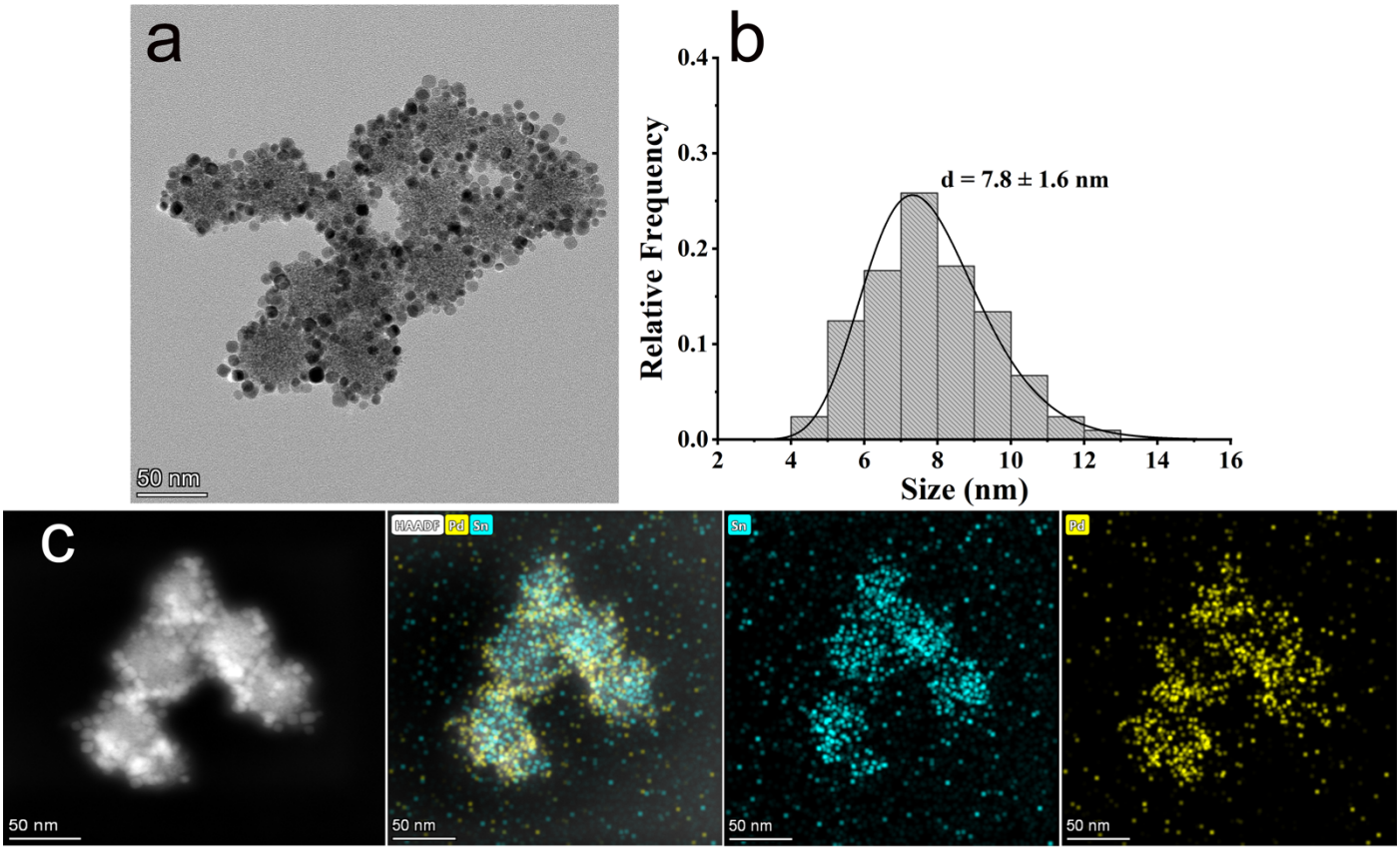

Fig. S2 (a) TEM image of *l*-PdNCs@SnO_2 nanocomposites. (b) Histogram showing the statistical size distribution of the PdNCs in *l*-PdNCs@SnO_2. (c) HAADF-STEM image of *l*-PdNCs@SnO_2 nanocomposites and the corresponding combined and separate EDX elemental mappings of Pd (yellow) and Sn (cyan).

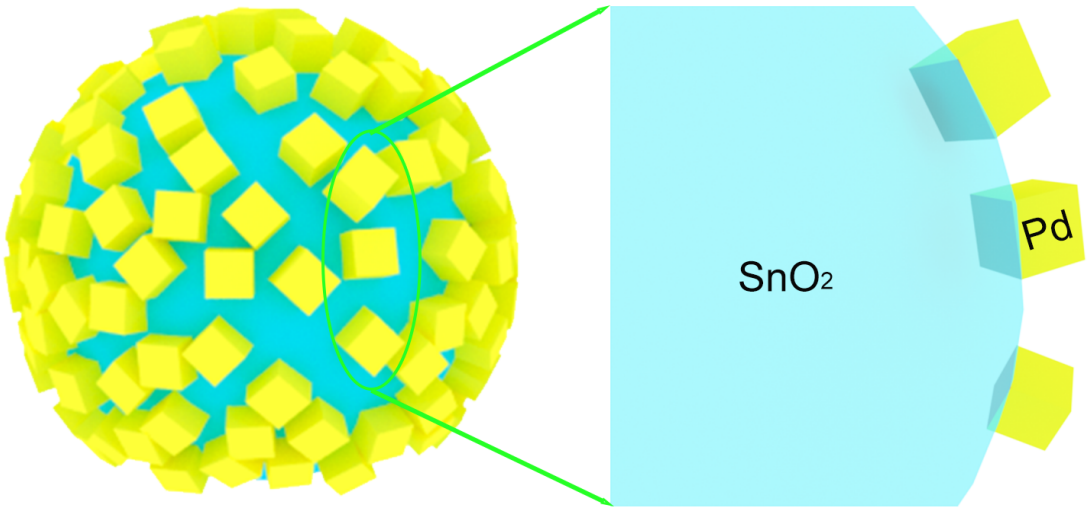

Fig. S3 Simplified model employed for calculation of the *surface coverage (θ)*.

To calculate the *surface coverage*, we used a simplified model wherein each PdNC contacts the SnO_2 sphere through one facet. Therefore, the *surface coverage* can be determined as the quotient of the total area of the contacting facets by the total surface area of SnO_2 nanospheres, which is shown below.

$$\theta = \frac{\frac{r}{\rho_1 d_1^3} \cdot d_1^2}{\frac{1}{\rho_2 \cdot \frac{4}{3}\pi\left(\frac{d_2}{2}\right)^3} \cdot 4\pi\left(\frac{d_2}{2}\right)^2} = \frac{r\rho_2 d_2}{6\rho_1 d_1}$$

Where, r is the mean mass ratio of Pd/SnO_2 which can be determined by ICP-OES; ρ_1 and ρ_2 are the mass density of Pd and SnO_2, respectively; d_1 and d_2 are the mean edge length of PdNCs and the mean diameter of SnO_2 nanospheres, respectively, which can be measured from the corresponding TEM image.

Note that the polycrystalline SnO_2 nanosphere in this work should have a smaller mass density than solid SnO_2. ρ_2 here adopted from the mass density of solid SnO_2 thus is overestimated, resulting in an overestimated surface coverage. Also, occasional isolated PdNCs (non-contacting with SnO_2 nanospheres) are also probed by the ICP-OES, which also makes the surface coverage overestimated.

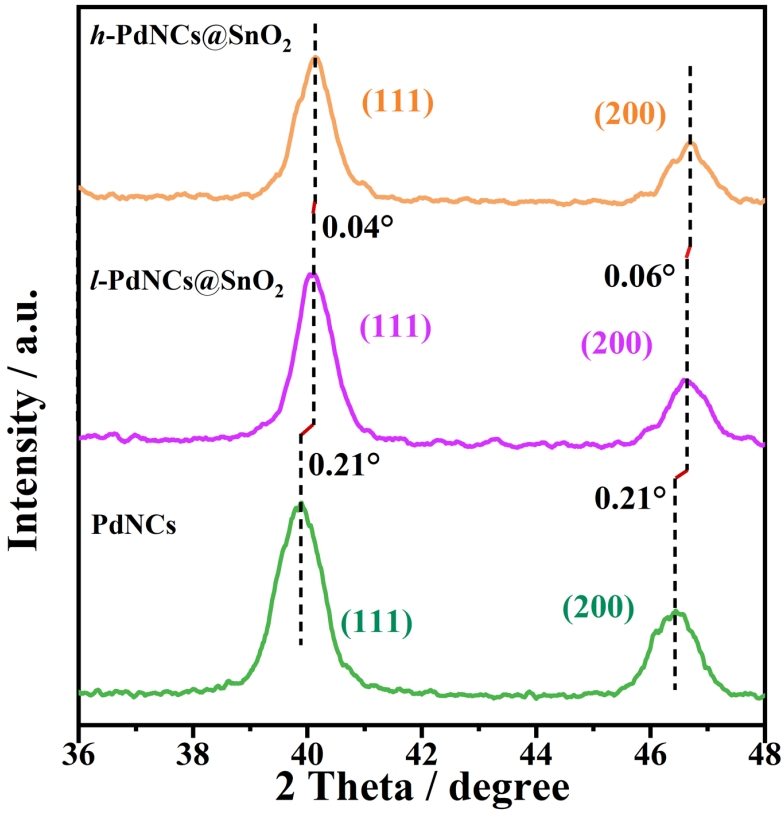

Fig. 4 A magnified view of the XRD patterns showing the Pd(111) and Pd(200) peaks of *h*, *l*-PdNCs@SnO_2 shift towards higher diffraction angles relative to those of PdNCs.

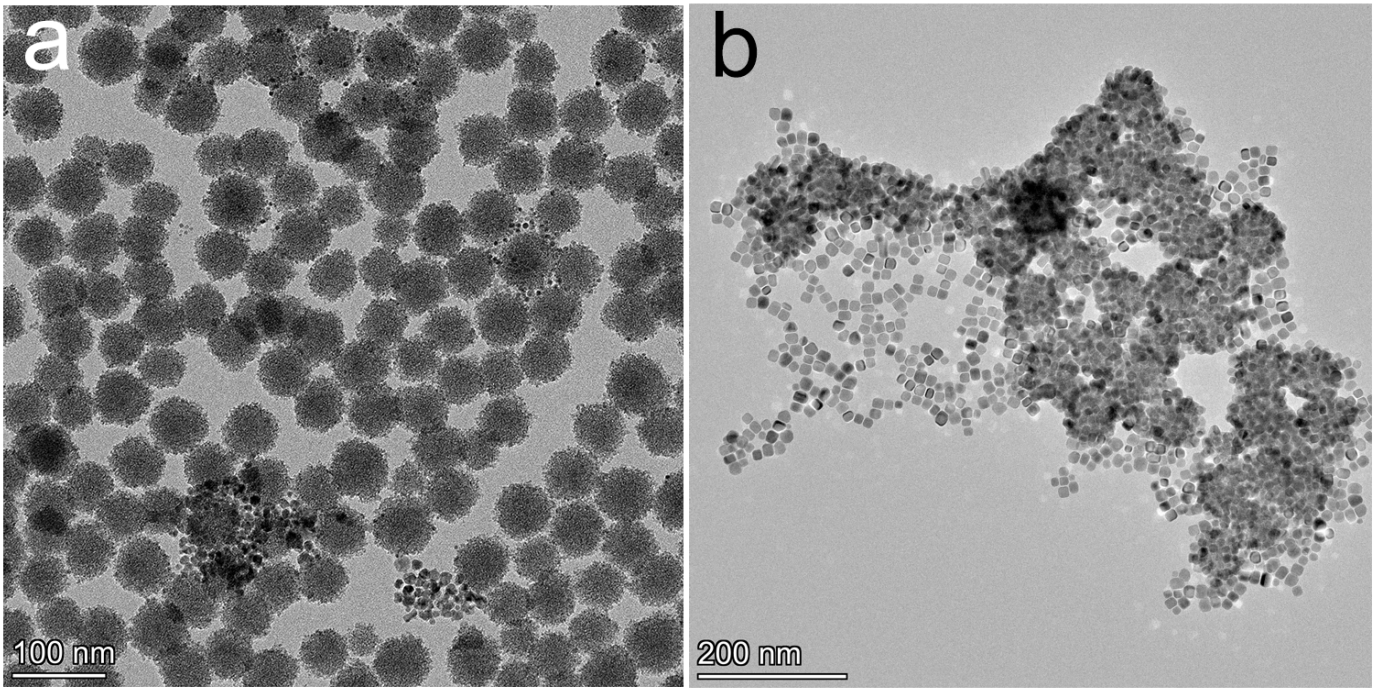

Fig. S5 TEM images of the Pd/SnO_2 composites formed at (a) 90 ℃ and (b) 150 ℃.

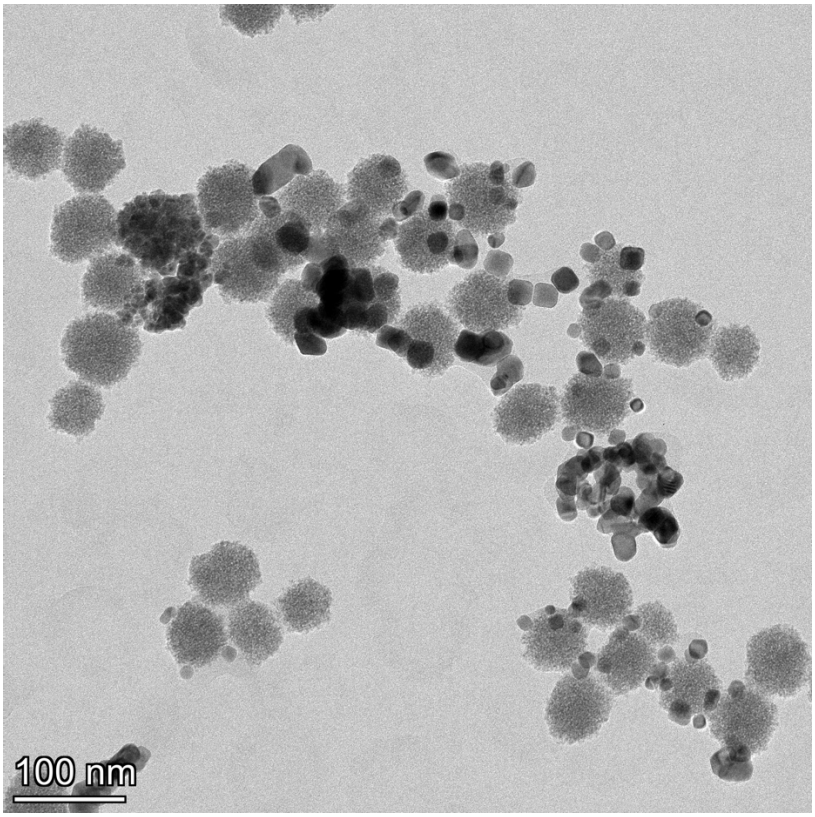

Fig. S6 TEM image of the Pd/SnO_2 composites formed using CTAB, instead of PVP, as the ligand.

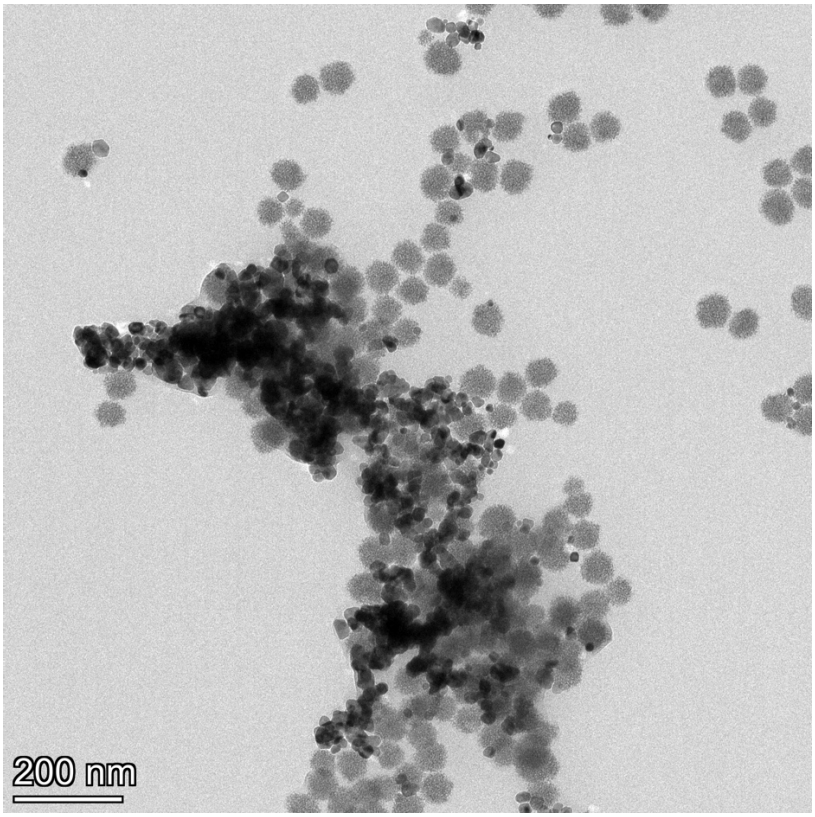

Fig. S7 TEM image of the Pd/SnO_2 composites formed using ascorbic acid, instead of DMF, as the reductant.

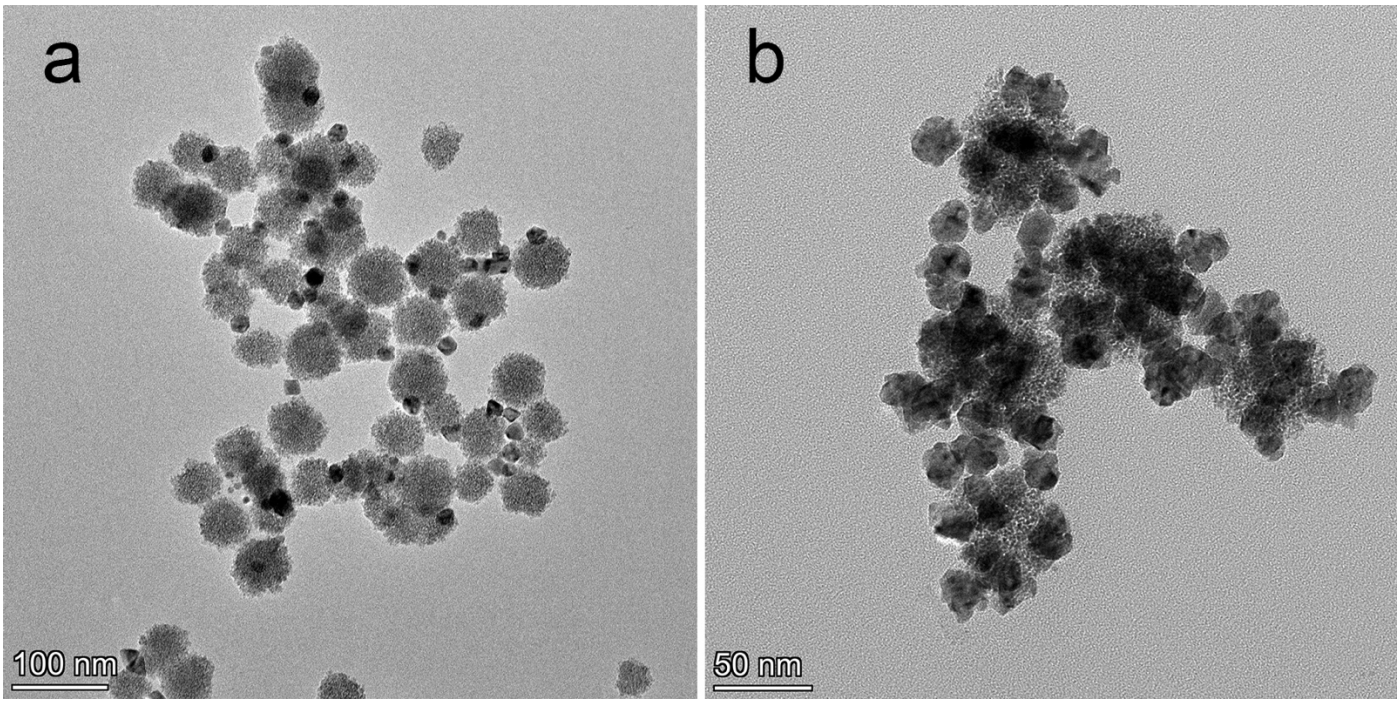

Fig. S8 (a, b) TEM images of the Pd/SnO_2 composites formed without using I^- ions as the capping agent after the (a) first and (b) second round growth.

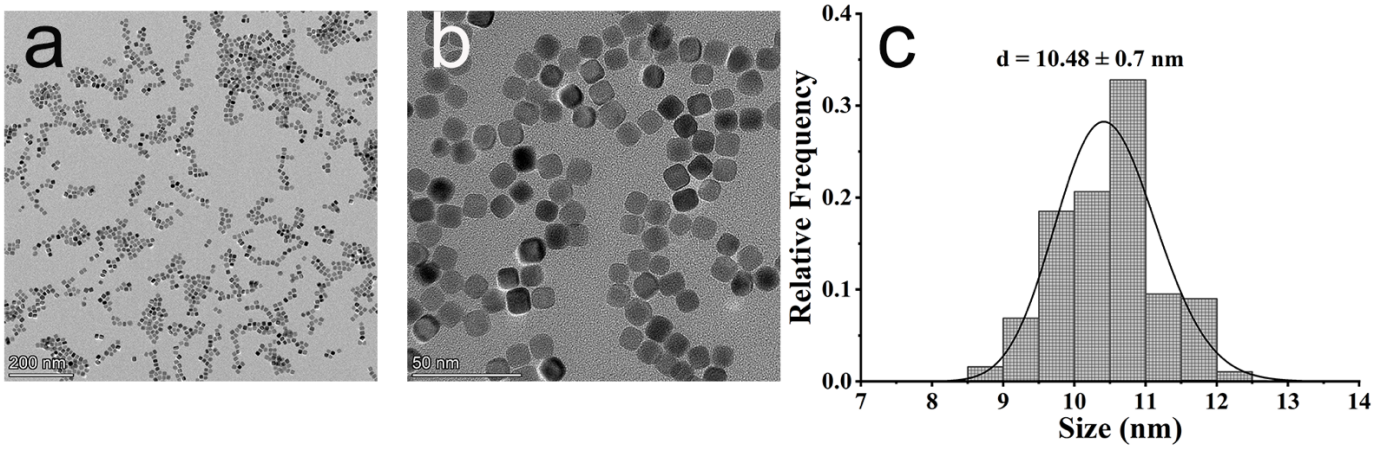

Fig. S9 (a) TEM and (b) HRTEM images of PdNCs. (c) Histogram showing the statistical size distribution of the PdNCs.

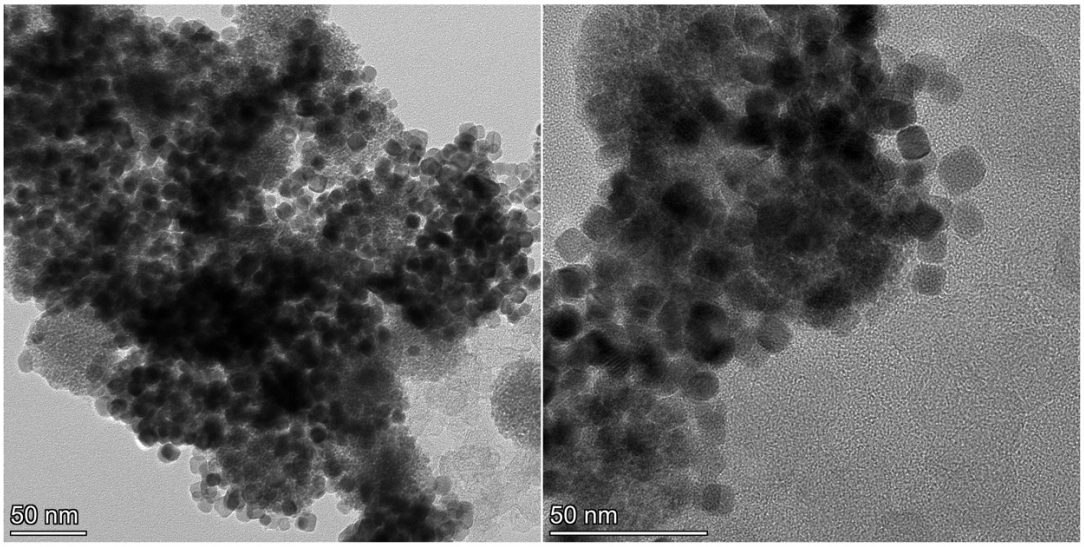

Fig. S10 TEM images of *h*-PdNCs@SnO_2 loaded on carbon after the ligand removal process, showing the conservation of particle morphology and architecture, while occasional presence of isolated Pd particles that might be detached from the SnO_2 spheres by the long ultrasonication during the preparation of the catalyst ink.

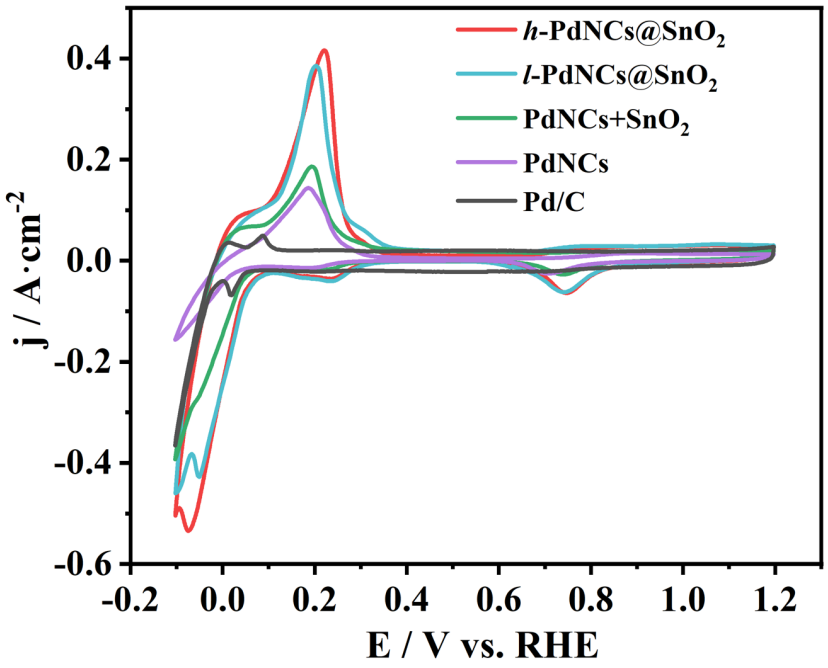

Fig. S11 CV profiles, reported in the form of geometric activity, of Pd/SnO_2 composites (*h*, *l*-PdNCs@SnO_2 and PdNCs+SnO_2) in comparison with PdNCs and Pd/C recorded in 1.0 M $HClO_4$ at 50 mV s^{-1}.

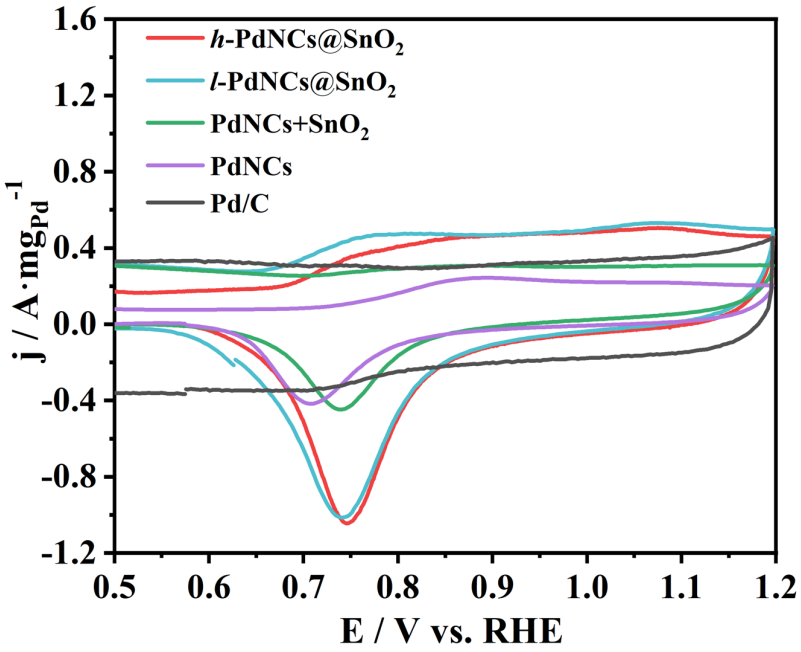

Fig. S12 Zoom-in view of the Pd oxidation/reduction region (>0.675 V) of the CV profiles presented in Fig. 3a.

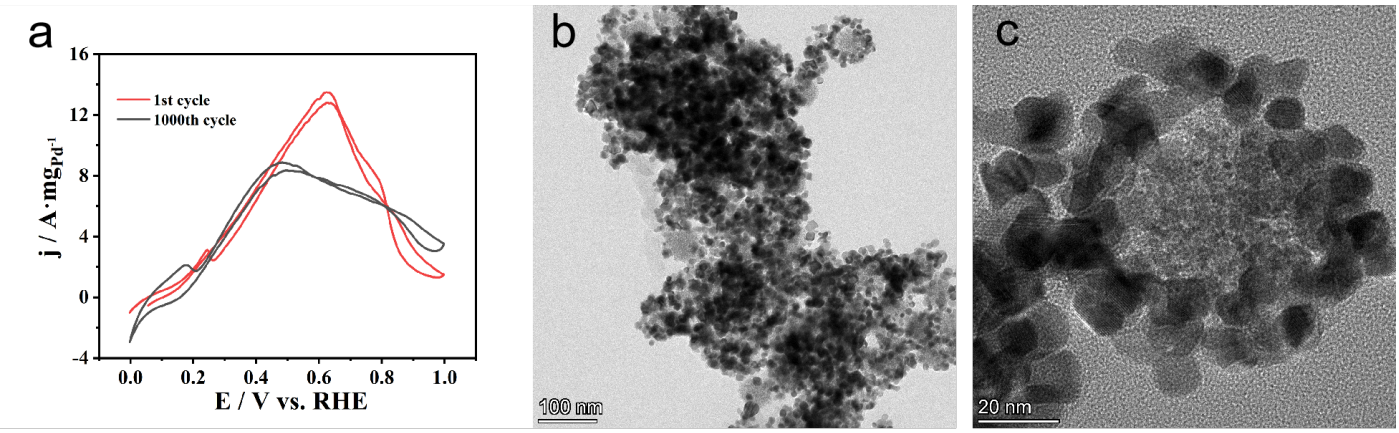

Fig. S13 (a) CV profiles of FAO on *h*-PdNCs@SnO_2 recorded at the 1st (red) and 1000th cycle (black) in 1.0 M $HClO_4$ + 0.5 M HCOOH at 50 mV s^{-1}. (b) TEM and (c) HRTEM image of *h*-PdNCs@SnO_2 after 1000 CV cycles.

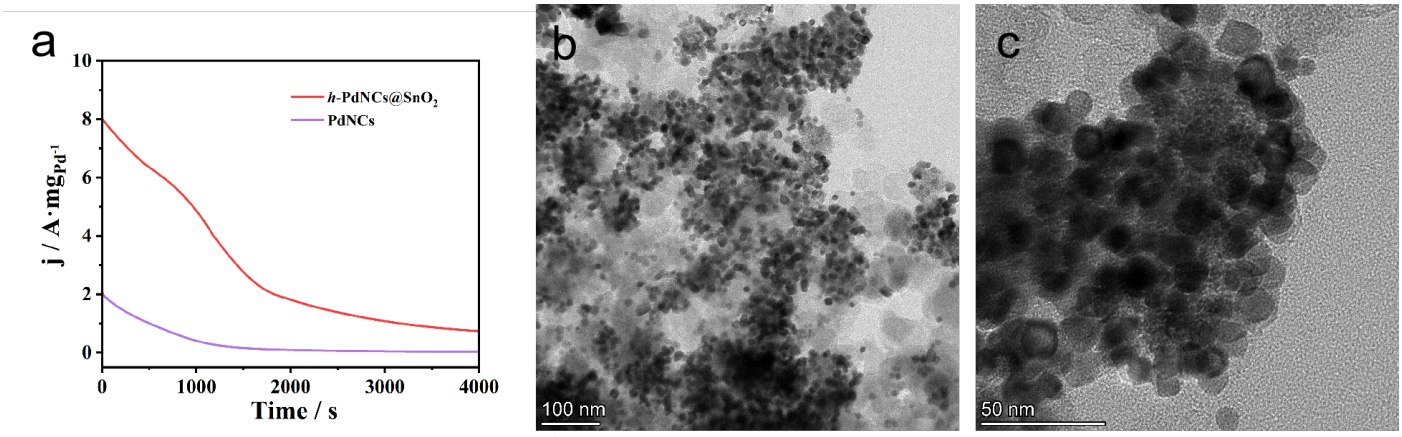

Fig. S14 (a) Chronoamperometric curves of FAO on *h*-PdNCs@SnO_2 (red) and PdNCs (purple) recorded at 0.35 V vs. RHE in 1.0 M $HClO_4$ + 0.5 M HCOOH. (b) TEM and (c) HRTEM images of *h*-PdNCs@SnO_2 after 4000 s - chronoamperometric test.

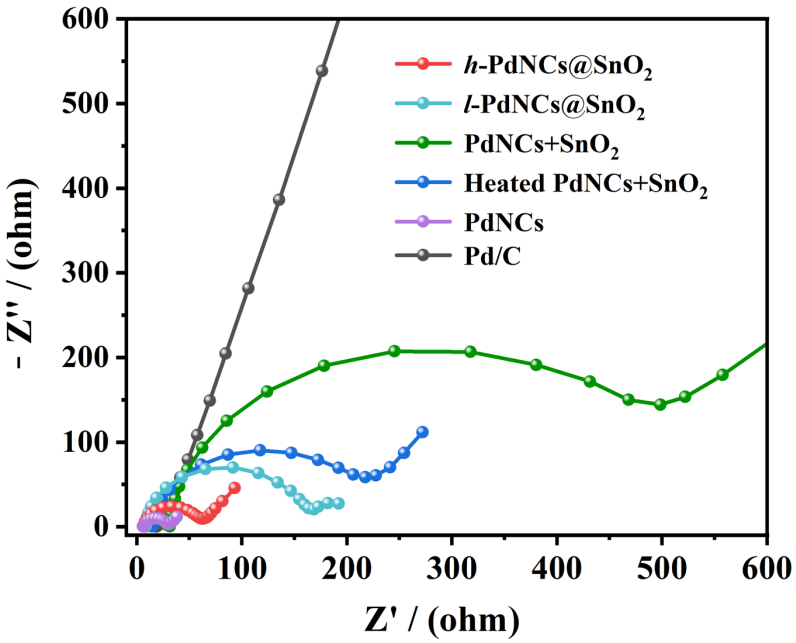

Fig. S15 EIS-Nyquist plots of Pd/C, PdNCs, PdNCs+SnO_2, Heated PdNCs+SnO_2 and *l*/*h*-PdNCs@SnO_2, obtained in 1.0 M $HClO_4$ + 0.5 M HCOOH at the open circuit potential.

Note: SnO_2 is much less conductive than Pd. As a result, the physically mixing of PdNCs with SnO_2 causes a significantly increased charge transfer resistance (R_{ct}) for PdNCs+SnO_2, relative to the original PdNCs. The Heated PdNCs+SnO_2 has an improved interfacial contact between PdNCs and SnO_2 and hence an improved conductivity or a decreased R_{ct} than PdNCs+SnO_2. As the interfacial contact becomes increasingly intimate, the conductivity can be further promoted, which is the case for *l*-PdNCs@SnO_2. *h*-PdNCs@SnO_2 possesses a larger density of intimate interfaces than *l*-PdNCs@SnO_2 and therefore, it shows an even lower R_{ct}.

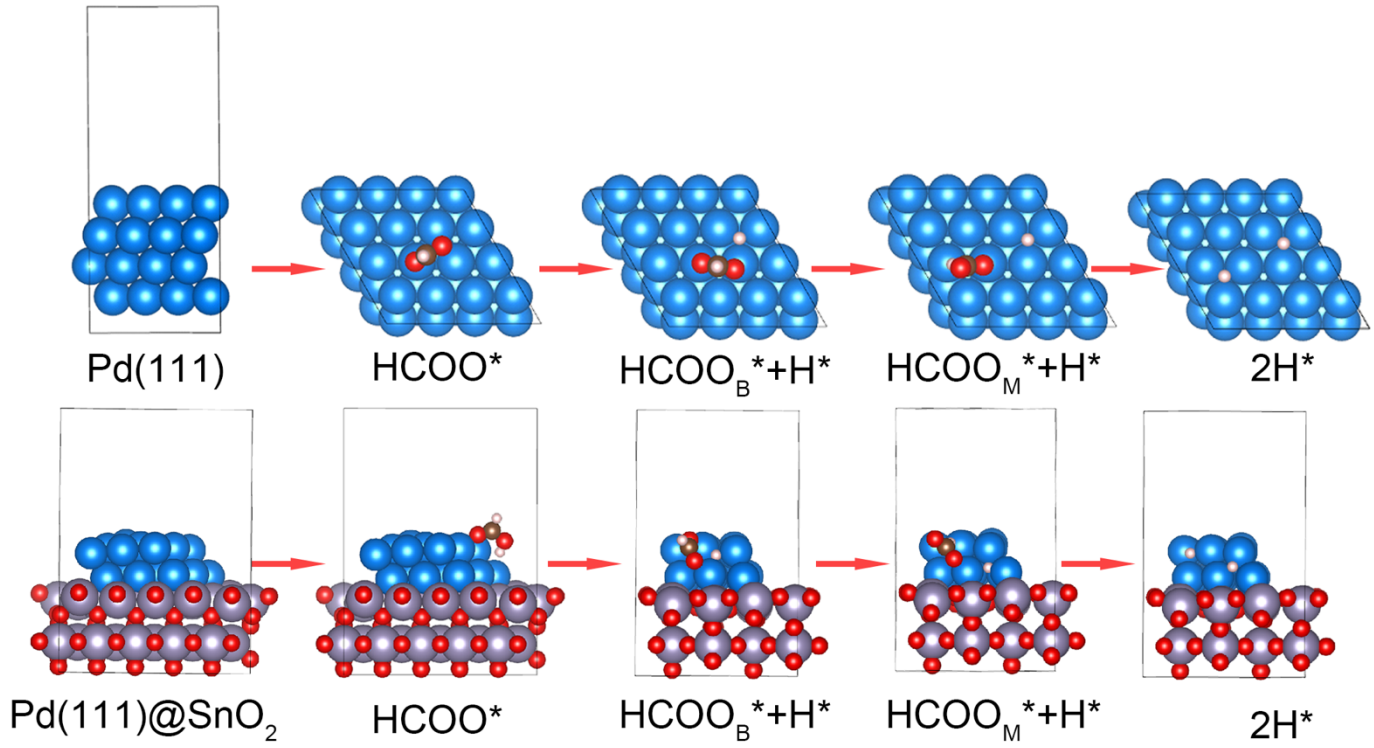

Fig. S16 Structures of adsorption sites and reaction intermediates for formic acid decomposition on Pd(111) and Pd(111)@SnO_2. The blue, grey, red, brown and white balls represent Pd, Sn, O, C and H, respectively.

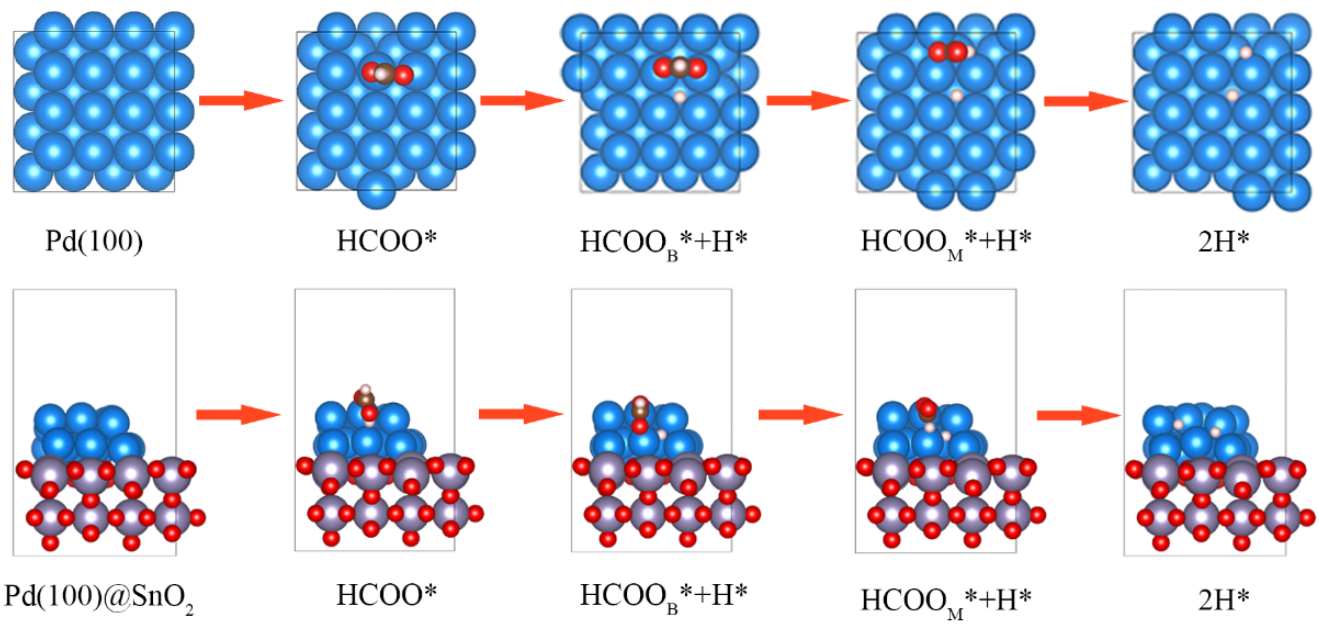

Fig. S17 Structures of adsorption sites and reaction intermediates for formic acid decomposition on Pd(100) and Pd(100)@SnO_2. The blue, grey, red, brown and white balls represent Pd, Sn, O, C and H, respectively.

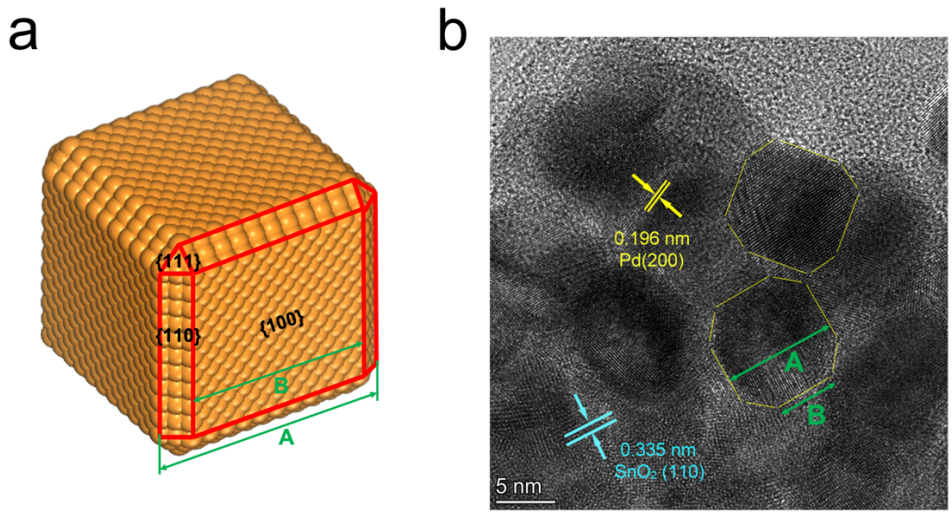

Fig. S18 (a) schematic model of a cube and (b) HR-TEM image of *h*-PdNCs@SnO_2.

As shown in **Fig. S18a**, the PdNCs consist of six {100} facets, twelve {110} edge facets and eight {111} corner facets. According to the schematic model, the {100}/{111} ratio can be calculated in the following way:

$$\frac{\{100\}}{\{111\}} = \frac{6 \times B^2}{8 \times [\frac{1}{2} \times Sin60° \times \left((\frac{A-B}{2})/Sin45°\right)^2]} = \frac{6 \times B^2}{\sqrt{3} \times (A-B)^2}$$

Where, *A* and *B* can be measured from the HR-TEM image of PdNCs (**Fig. S18b**).

On the basis of more than 50 particles of PdNCs in *h*-PdNCs@SnO_2 (A = 10.3 nm, B = 7.6 nm) and *l*-PdNCs@SnO_2 (A = 7.8 nm, B = 5.6 nm), we obtained the {100}/{111} ratios as follows:

- *h*-PdNCs@SnO_2: {100}/{111} = 27.4
- *l*-PdNCs@SnO_2: {100}/{111} = 22.4

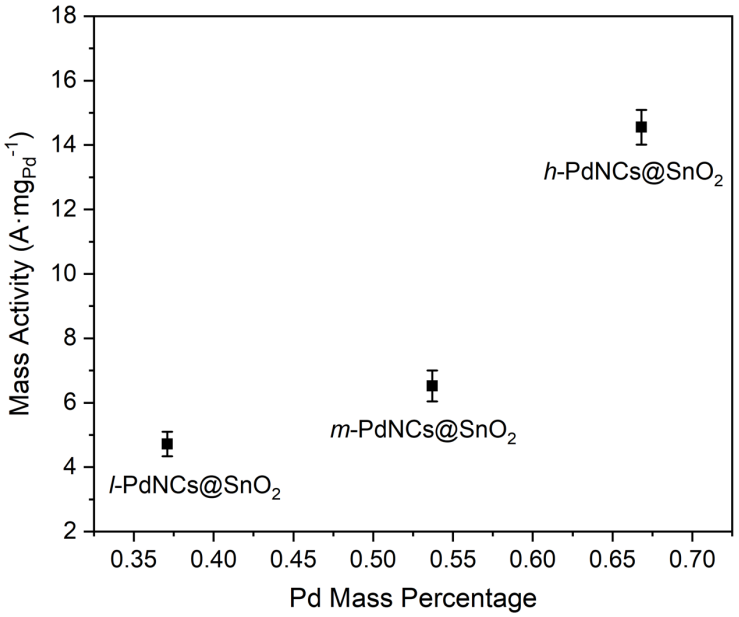

Fig. S19 Pd loading-dependent mass activity of PdNCs@SnO_2 nanocomposites. The error bars show standard deviations from three independent measurements.

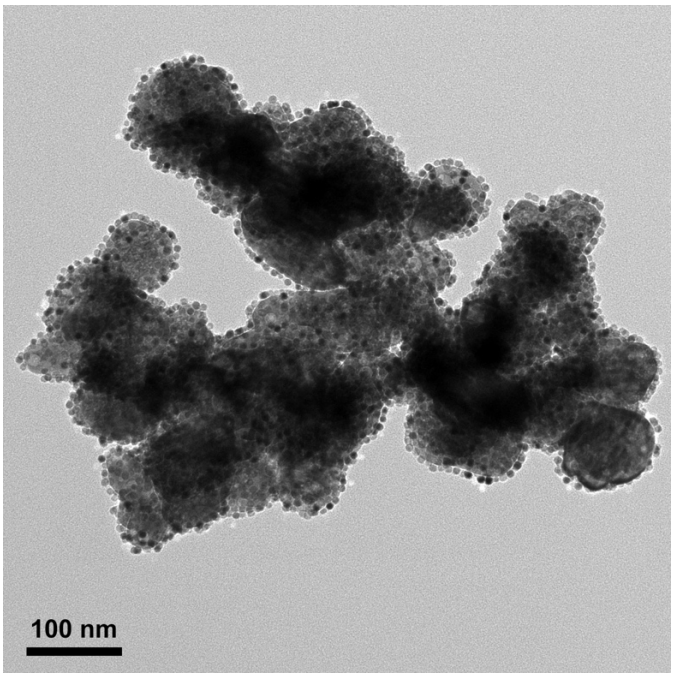

Fig. S20 TEM image of PdNCs/In_2O_3 nanocomposites prepared using the similar approach reported in this work, which demonstrates the extendibility of the synthetic strategy.

Supporting Tables

Table S1. Comparison of mass activity at the peak potential between *h, l*-PdNCs@SnO_2 and reported state-of-the-art Pd-based electrocatalysts.[6-40] Catalysts quoted in Fig. 3c are highlighted in grey in this table.

Catalysts	Electrolytes	Peak potential /V vs. RHE	Mass activity / A·mg_{Pd}^{-1}	Specific activity /mA·cm^{-2}	ECSA /m^2·g^{-1}	Ref.
h-PdNCs@SnO_2	1.0 M $HClO_4$ + 0.5 M HCOOH	0.55	14.55	27.24	52.38	This work
l-PdNCs@SnO_2	1.0 M $HClO_4$ + 0.5 M HCOOH	0.61	4.72	17.14	26.84	This work
PdCo single atom layer	0.5 M $HClO_4$ + 0.5 M HCOOH	0.3	2.93	NA	247	6
$Pd_{87}Cu_{13}$	0.5 M $HClO_4$ + 0.5 M HCOOH	0.54	1.58	5.51	NA	7
$Pd_{0.6}/WO_{2.72}$	0.1 M $HClO_4$ + 1.0 M HCOOH	0.62	1.618	NA	NA	8
C-$Cu_{48}Pd_{52}/WO_{2.72}$	0.1 M $HClO_4$ + 1.0 M HCOOH	0.8	2.086	NA	NA	9
3D-RGO/Pd-networks	0.5 M H_2SO_4 + 0.5 M HCOOH	0.40	0.9724	2.6	39.3	10
PdAg/$Ti_{0.5}Cr_{0.5}N$	0.1 M $HClO_4$ + 1.0 M HCOOH	0.64	0.975	NA	NA	11
SnO_2@Pd nanocubes	0.1 M $HClO_4$ + 0.5 M HCOOH	0.55	2.46	NA	NA	12
Pd@SnO_2 nanosheet	1.0 M $HClO_4$ + 0.5 M HCOOH	0.45	4.96	21.695	22.86	13
Pd/CeO_2/C	0.1 M $HClO_4$ + 0.5 M HCOOH	0.6	2.4	4.6	52.6	14
Pd/FeP-250	0.5 M H_2SO_4 + 0.5 M HCOOH	0.58	1.54	110	90	15
Pd/TiO_2/CNT	0.1 M $HClO_4$ + 0.5 M HCOOH	0.77	2.6	4.8	54.2	16
PdIr Bimetallene	0.1 M $HClO_4$ + 0.5 M HCOOH	0.5	2.7	NA	127.5	17
β-PdH Nanocrystals	0.5 M $HClO_4$ + 0.5 M HCOOH	β-PdH cubes: 0.66 β-PdH octahedra: 0.61	β-PdH cubes: 4.4 β-PdH octahedra: 3.53	β-PdH cubes: 7.48 β-PdH octahedra: 5.80	β-PdH cubes: 58.8 β-PdH octahedra: 60.5	18
PdBP Nanorod	0.5 M H_2SO_4 + 0.5 M HCOOH	0.7	1.32	4.58	20.17	19

Pd nanosheets	0.1 M $HClO_4$ + 0.2 M HCOOH	0.66	0.6343	NA	35.6	20
POM-Pd-20-P01	0.5 M H_2SO_4 + 0.5 M HCOOH	0.24 (vs. SCE)	3.34	3.6	90.5	21
P-PdNTA	0.5 M H_2SO_4 + 0.5 M HCOOH	0.3 (vs. SCE)	3.65	4.41	82.7	22
P-Pd nanosheets	0.5 M H_2SO_4 + 0.5 M HCOOH	0.23 (vs. SCE)	2.6533	1.55	172.6	23
PdCu alloy nanosheets	0.5 M H_2SO_4 + 0.25 M HCOOH	0.12 (vs. SCE)	1.6557	NA	139.8	24
Cu_3PdN NPs	0.5 M H_2SO_4 + 0.5 M HCOOH	0.24 (vs. SCE)	0.87	NA	NA	25
Pd_xNi/rGO	0.5 M H_2SO_4 + 0.5 M HCOOH	0.196 (vs. SCE)	1.435	NA	NA	26
Pd_3Au	0.1 M $HClO_4$ + 0.1 M HCOOH	0.2 (vs. SCE)	0.52055	18.11	95.68	27
PdAg-100/GC	0.1 M $HClO_4$ + 0.5 M HCOOH	0.285 (vs. SCE)	NA	3.82	NA	28
Pd_2Sn_1	0.5 M H_2SO_4 + 0.5 M HCOOH	0.3 (vs. SCE)	1.35	5.458	24.64	29
PdBi nanodot	0.5 M H_2SO_4 + 0.5 M HCOOH	0.4 (vs. SCE)	1.6285	NA	53.2	30
PdSn-INNs	0.5 M H_2SO_4 + 0.5 M HCOOH	0.21 (vs. SCE)	0.5537	2.975	18.6	31
PdRuBP NAs	0.5 M H_2SO_4 + 0.5 M HCOOH	0.42 (vs. SCE)	1.71	4.51	49.24	32
Pd/THPP	0.1 M H_2SO_4 + 0.1 M HCOOH	0.1 (vs. SCE)	4.65	NA	168	33
Pd/PG	0.5 M H_2SO_4 + 0.5 M HCOOH	0.285 (vs. SCE)	1.0457	84.7	103.8	34
Pd_1Bi_1/NG	0.5 M H_2SO_4 + 0.5 M HCOOH	0.38 (vs. SCE)	2.0255	7.85	26.83	35
2D porous Pd nanosheets	0.5 M H_2SO_4 + 0.5 M HCOOH	0.175 (vs. SCE)	0.4093	NA	12.9	36
$Au_{core}@Pd_{shell}$	0.5 M H_2SO_4 + 0.5 M HCOOH	$Au_{71}Pd_{29}$: 0.22 (vs. SCE) $Au_{56}Pd_{44}$: 0.23 (vs. SCE)	$Au_{71}@Pd_{29}$: 1.405 A mg_{Pd}^{-1} $Au_{56}@Pd_{44}$: 1.160 A mg_{Pd}^{-1}	$Au_{71}@Pd_{29}$: 2.167 $Au_{56}@Pd_{44}$: 2.333	$Au_{71}@Pd_2$: 64.84 $Au_{56}@Pd_{44}$: 49.72	37
Pd_4Sn NCNs	0.5 M H_2SO_4 + 0.5 M HCOOH	0.172 (vs. SCE)	0.8504	32.7	119.4	38

L-Pd/PdWCr	0.5 M H_2SO_4 + 0.5 M HCOOH	0.14 (vs. SCE)	2.087	NA	89.1	39
PdNi-HNCs	0.5 M H_2SO_4 + 0.5 M HCOOH	0.31 (vs. SCE)	0.768	2.76	19.74	40

Table S2. Calculated change of reaction free energy (ΔG) for the different steps over modelled $Pd(111)@SnO_2$, Pd(111), $Pd(100)@SnO_2$ and Pd(100)

Reactions	ΔG / eV			
	$Pd(111)@SnO_2$	**Pd(111)**	**$Pd(100)@SnO_2$**	**Pd(100)**
HCOOH → HCOOH*	–0.16	–0.02	–0.17	–0.12
HCOOH* → $HCOO_B$* + H*	–0.32	–0.51	–0.12	–0.12
$HCOO_B$* →$HCOO_M$*	0.25	0.54	0.16	0.35
$HCOO_M$* → CO_2* + H*	–0.48	–1.22	–1.15	–1.14

Supporting References

1. G. Kresse and J. Furthmuller, *Physical Review B: Condensed Matter*, 1996, **54**, 11169-11186.
2. J. P. Perdew, K. Burke and M. Ernzerhof, *Physical Review Letters*, 1996, **77**, 3865-3868.
3. P. E. Blochl, *Physical Review B: Condensed Matter*, 1994, **50**, 17953-17979.
4. I. L. Garzón and A. Posada-Amarillas, *Physical Review B*, 1996, **54**, 11796-11802.
5. J. K. Nørskov, J. Rossmeisl, A. Logadottir, L. Lindqvist, J. R. Kitchin, T. Bligaard and H. Jónsson, *Journal of Physical Chemistry B*, 2004, **108**, 17886-17892.
6. J. X. Jiang, W. Ding, W. Li and Z. D. Wei, *Chem*, 2020, **6**, 1-17.
7. L. Zhang, S. I. Choi, J. Tao, H. C. Peng, S. F. Xie, Y. M. Zhu, Z. X. Xie and Y. N. Xia, *Advanced Functional Materials*, 2014, **24**, 7520-7529.
8. Z. Xi, D. P. Erdosy, A. Mendoza-Garcia, P. N. Duchesne, J. Li, M. Muzzio, Q. Li, P. Zhang and S. Sun, *Nano Letters*, 2017, **17**, 2727-2731.
9. Z. Xi, J. Li, D. Su, M. Muzzio, C. Yu, Q. Li and S. Sun, *Journal of the American Chemical Society*, 2017, **139**, 15191-15196.
10. X. Y. Qiu, P. Wu, L. Xu, Y. W. Tang and J. M. Lee, *Advanced Materials Interfaces*, 2015, **2**, 1500321.
11. Z. Cui, M. Yang and F. J. DiSalvo, *ACS Nano*, 2014, **8**, 6106-6113.
12. C. Rettenmaier, R. M. Aran-Ais, J. Timoshenko, R. Rizo, H. S. Jeon, S. Kuhl, S. W. Chee, A. Bergmann and B. Roldan Cuenya, *ACS Catalysis*, 2020, **10**, 14540-14551.
13. Y. W. Zhou, Y. F. Chen, X. X. Qin, K. Jiang, W. F. Lin and W. B. Cai, *Journal of Catalysis*, 2021, **399**, 8-14.
14. W. J. Shi, A. H. Park, H. U. Park and Y. U. Kwon, *Journal of Catalysis*, 2020, **384**, 22-29.
15. Y. F. Bao, H. Liu, Z. Liu, F. L. Wang and L. G. Feng, *Applied Catalysis B: Environmental*, 2020, **274**, 119106.
16. W. Shi, A. H. Park, S. Xu, P. J. Yoo and Y. U. Kwon, *Applied Catalysis B: Environmental*, 2021, **284**, 119715.
17. F. Lv, B. Huang, J. Feng, W. Zhang, K. Wang, N. Li, J. Zhou, P. Zhou, W. Yang, Y. Du, D. Su and S. Guo, *National Science Review*, 2021, **8**, nwab019.
18. M. K. Kabiraz, J. Kim, W.-J. Lee, B. Ruqia, H. C. Kim, S.-U. Lee, J.-R. Kim, S.-M. Paek, J. W. Hong and S.-I. Choi, *Chemistry of Materials*, 2019, **31**, 5663-5673.
19. Y. Xu, M. Z. Wang, S. S. Yu, T. L. Ren, K. L. Ren, Z. Q. Wang, X. N. Li, L. Wang and H. J. Wang, *Chemical Engineering Journal*, 2021, **421**, 127751.
20. Y. Zhang, M. Wang, E. Zhu, Y. Zheng, Y. Huang and X. Huang, *Nano Letters*, 2015, **15**, 7519-7525.
21. J. Ding, Z. Liu, X. Liu, B. Liu, J. Liu, Y. Deng, X. Han, W. Hu and C. Zhong, *Angewandte Chemie International Edition*, 2020, **132**, 5130 – 5139.
22. J. Ding, Z. Liu, X. R. Liu, J. Liu, Y. D. Deng, X. P. Han, C. Zhong and W. B. Hu, *Advanced Energy Materials*, 2019, **9**, 1900955.
23. Y. O. Lian Ying Zhang, Shuo Wang, Diben Wu, Mengchao Jiang, Fengqian Wang, Weiyong Yuan, and Chang Ming Li, *Small*, 2019, **15**, 1904245.
24. N. Yang, Z. Zhang, B. Chen, Y. Huang, J. Chen, Z. Lai, Y. Chen, M. Sindoro, A. L. Wang, H. Cheng, Z. Fan, X. Liu, B. Li, Y. Zong, L. Gu and H. Zhang, *Advanced Materials*, 2017, **29**, 1700769.
25. J. Jia, M. Shao, G. Wang, W. Deng and Z. Wen, *Electrochemistry Communications*, 2016, **71**, 61-64.
26. M. Y. Li, R. Q. Liu, G. Y. Han, Y. N. Tian, Y. Z. Chang and Y. M. Xiao, *Chinese Journal of Chemistry*, 2017, **35**, 1405-1410.
27. S.-Y. Lee, N. Jung, J. Cho, H.-Y. Park, J. Ryu, I. Jang, H.-J. Kim, E. Cho, Y.-H. Park, H. C. Ham, J.

H. Jang and S. J. Yoo, *ACS Catalysis*, 2014, **4**, 2402-2408.
28. Y. Lu and W. Chen, *The Journal of Physical Chemistry C*, 2010, **114**, 21190-21200.
29. Q. Qin, J. Xie, Q. Z. Dong, G. Yu and H. Chen, *New Journal of Chemistry*, 2019, **43**, 19242-19252.
30. H. Xu, K. Zhang, B. Yan, J. Wang, C. Q. Wang, S. M. Li, Z. L. Gu, Y. K. Du and P. Yang, *Journal of Power Sources*, 2017, **356**, 27-35.
31. D. Sun, L. Si, G. Fu, C. Liu, D. Sun, Y. Chen, Y. Tang and T. Lu, *Journal of Power Sources*, 2015, **280**, 141-146.
32. Y. Xu, S. Yu, T. Ren, C. Li, S. Yin, Z. Wang, X. Li, L. Wang and H. Wang, *Journal of Materials Chemistry A*, 2020, **8**, 2424-2429.
33. X. Wang, J. Yang, H. Yin, R. Song and Z. Tang, *Advanced Materials*, 2013, **25**, 2728-2732.
34. J. Zhao, Z. Liu, H. Li, W. Hu, C. Zhao, P. Zhao and D. Shi, *Langmuir*, 2015, **31**, 2576-2583.
35. H. Xu, B. Yan, K. Zhang, J. Wang, S. M. Li, C. Q. Wang, Y. K. Du, P. Yang, S. J. Jiang and S. Q. Song, *Applied Surface Science*, 2017, **416**, 191-199.
36. X. Y. Qiu, H. Y. Zhang, P. S. Wu, F. Q. Zhang, S. H. Wei, D. M. Sun, L. Xu and Y. W. Tang, *Advanced Functional Materials*, 2017, **27**, 1603852.
37. L. Yang, G. Li, J. Chang, J. Ge, C. Liu, F. Vladimir, G. Wang, Z. Jin and W. Xing, *Applied Catalysis B: Environmental*, 2020, **260**, 118200.
38. Y. Gong, X. Liu, Y. Gong, D. Wu, B. Xu, L. Bi, L. Y. Zhang and X. S. Zhao, *Journal of Colloid and Interface Science*, 2018, **530**, 189-195.
39. L. Y. Zhang, F. Q. Wang, S. Wang, H. W. Huang, X. M. Meng, Y. R. Ouyang, W. Y. Yuan, C. X. Guo and C. M. Li, *Advanced Functional Materials*, 2020, **30**, 2003933.
40. Z. L. Chen, J. F. Zhang, Y. Zhang, Y. W. Liu, X. P. Han, C. Zhong, W. B. Hu and Y. D. Deng, *Nano Energy*, 2017, **42**, 353-362.